*Article*

# A Self-Assembled AMF-Responsive Nanoplatform Based on Pillar[5]arene and Superparamagnetic Nanoparticles for Controlled Release of Doxorubicin

*Tamires S. Fernandes,[a] Evelyn C. S. Santos,[a,b] Vinicius G. C. Madriaga,[a] Isabela A. A. Bessa,[a] Vanessa Nascimento,[a] Flávio Garcia[b] and Célia M. Ronconi* [ID] *,[a]*

[a]*Departamento de Química Inorgânica, Universidade Federal Fluminense, Campus do Valonguinho, Outeiro São João Batista s/n, Centro, 24020-150 Niterói-RJ, Brazil*

[b]*Centro Brasileiro de Pesquisas Físicas (CBPF), Rua Dr Xavier Sigaud 150, Urca, 22290-180 Rio de Janeiro-RJ, Brazil*

An alternating magnetic field (AMF)-stimuli responsive nanodevice based on magnetic nanoparticles (MNP) functionalized with water-soluble carboxylate-substituted pillar[5]arene (CP[5]A), namely MNP-CP[5]A, as a multiplatform for cancer treatment has been designed. MNP-CP[5]A was loaded with doxorubicin (DOX), showing a loading capacity of 9.5 mg g$^{-1}$. The nanodevice demonstrated good colloidal stability, superparamagnetic behavior, and was capable to generate detectable heat in solution induced by AMF application. DOX release, monitored by ultraviolet-visible (UV-Vis) spectroscopy, was investigated by varying the temperature (37 and 45 °C) without AMF and in the presence of AMF (frequency (f) = 307 kHz, field amplitude (H) = 200 Oe, 45 °C) at pH = 7.4. Thermo-induced DOX release without AMF was 1.9% (1.8 μg mL$^{-1}$) and 2.3% (3.3 μg mL$^{-1}$) at 37, and 45 °C within 50 min, respectively. In an AMF DOX release increased to 5.7% (8.2 μg mL$^{-1}$) within 50 min. Therefore, MNP-CP[5]A-DOX works as a chemo-hyperthermia nanodevice.

**Keywords:** carboxylate-substituted pillar[5]arene, superparamagnetic nanoparticles, magnetic hyperthermia, doxorubicin delivery, cancer

## Introduction

The most used treatments for cancer cells are chemotherapy and radiotherapy; however, they lead to undesirable side effects. Hyperthermia is an alternative treatment, in which the cancer cells are killed or damaged by exposing body tissues to high temperatures (up to 45 °C).[1] Cancer cells are more sensitive to temperature increase than the healthy ones because their disorganized and compact vascular structures are unable to dissipate heat efficiently.[2] Such treatment can be applied to different body extensions, ranging from small cell volumes to organs, and even the whole body.[3,4] The necessary heat can be generated by different approaches, e.g. ultrasound, microwaves, near-infrared radiation, or alternated magnetic field.[1,3-6]

Magnetic nanoparticles for hyperthermia-based therapy are gaining attention in the biomedical field.[7-9] In the treatment using magnetic hyperthermia (MH), the heat is locally generated when hyperthermia-inducing agents, such as magnetic nanoparticles (MNP) are submitted to an alternating magnetic field (AMF) of appropriate frequency and amplitude.[10] The advantages of MH in cancer treatment are that AMF penetration is deeper than any other stimulus and avoids body tissues damage caused by the ionizing radiation. Moreover, this modality is potentially selective to tumor cells and can be used as a combinatory treatment improving the effects of radiotherapy or chemotherapy.[3,11,12]

Among hyperthermia-inducing nanomaterials, superparamagnetic iron oxide nanoparticles (SPIONs)[13,14] are considered the best candidates because they are biocompatible and show a zero residual magnetization in the absence of an external magnetic field. The superparamagnetic behavior along with appropriate coating of the nanoparticles can avoid thrombosis caused by their agglomeration.[15] Moreover, iron oxide nanoparticles have the approval of U.S. Food and Drug Administration (FDA) for biomedical applications.[16,17]

Coating bare SPIONs with biocompatible materials to avoid aggregation and consequently guarantee the stability of colloidal dispersions is an important step in the design of efficient nanocarriers.[18] To address this issue, several inorganic and organic materials can be

*e-mail: cmronconi@id.uff.br

used to cover nanoparticles surface, such as silica,[19-21] citric acid,[14,22] dextran,[23] and macrocycles.[24-29] Recently, pillar[n]arenes (P[n]A), a new class of macrocycles derived from paracyclophanes, have emerged as biocompatible components for drug delivery systems and for many other biological applications.[30,31] The electron-rich cavity and possible chemical modification on the upper and lower rims of P[n]A can provide very useful water-soluble macrocycles with hydrophobic voids.[32] Thus, anionic and cationic water-soluble pillar[n]arenes have been widely explored as hosts for chemotherapeutic drugs[33,34] as well as micelles,[35,36] vesicles,[36-41] and gatekeepers in nanovalve systems.[42-47]
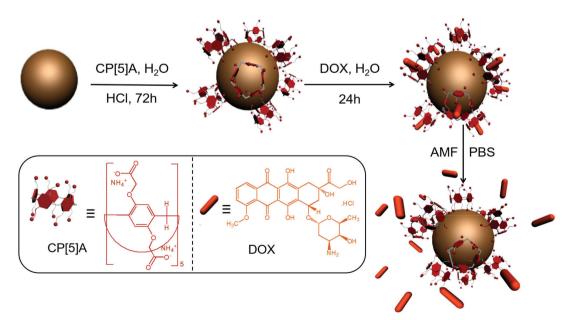
To the best of our knowledge, the combination of water-soluble carboxylate-substituted pillar[5]arene (CP[5]A) grafted onto SPIONs as an AMF stimuli-responsive nanodevice for drug delivery has not been described in the literature. Magnetite coated with CP[5]A has been reported for environmental applications, such as dye separation,[48] pesticide detection in beverages,[49] and used as gatekeepers in nanovalves for hormone delivery to plants.[47] For biomedical applications, SPIONs coated with metal-organic frameworks (MOFs) have been used as reservoir for fluorouracil (an anticancer drug), gated with carboxylate-substituted pillar[6]arene (CP[6]A) and investigated as a theranostic nanoplatform.[50]

Therefore, our goal in this work is to develop a novel chemo-hyperthermia nanodevice based on water-soluble carboxylate-substituted pillar[5]arene CP[5]A and SPIONs, namely MNP-CP[5]A (Scheme 1). The interaction between the anticancer drug (doxorubicin, DOX) and CP[5]A has not been reported in the literature

and, in this work, we investigated it by ^{1}H nuclear magnetic resonance (NMR) spectroscopy and the stoichiometry of the interaction was evaluated by the method of continuous variation (Job plot). The nanodevice was successfully prepared in three steps (Scheme 1): (*i*) synthesis of carboxylate-substituted pillar[5]arene (CP[5]A); (*ii*) synthesis of SPIONs using coprecipitation method; and (*iii*) functionalization of SPIONs with CP[5]A. The final material (MNP-CP[5]A) and their precursors were characterized by several techniques and loaded with doxorubicin (DOX). DOX release studies were carried out in phosphate buffered saline (PBS, pH 7.4) without AMF application at 37 (body temperature) and 45 °C (hyperthermia temperature), and also in the presence of AMF at 45 °C.

## Experimental

### Materials and methods

The reagents and solvents were used as received: 1,4-dimethoxybenzene (99%), paraformaldehyde (practical grade, p.a.), boron trifluoride diethyl etherate (p.a.), boron tribromide (≥ 99%), ethyl bromoacetate (98%), potassium iodide (≥ 99%), iron(II) chloride tetrahydrate (≥ 99%), iron(III) chloride anhydrous (≥ 97%), doxorubicin hydrochloride (98%), potassium nitrate (≥ 99%), sodium phosphate dibasic (98%), and potassium phosphate monobasic (98%) were purchased from Sigma-Aldrich (St. Louis, USA). All solvents, potassium carbonate (p.a.), ammonium hydroxide (30-34%), hydrochloric acid (37%),



**Scheme 1.** Representation of the preparation of MNP-CP[5]A-DOX nanodevice and doxorubicin (DOX) release in the presence of an alternating magnetic field (AMF).

nitric acid (≥ 65%) were purchased from Vetec (Rio de Janeiro, Brazil).

$^1$H and $^{13}$C nuclear magnetic resonance (NMR) spectra of the ammonium carboxylate-substituted pillar[5]arene salt were measured at room temperature (RT) on a Varian VNMRS at 500 and 125 MHz, respectively, using residual solvent as internal standards. The sample was prepared using $D_2O$ purchased from Cambridge Isotope Laboratories (Tewksbury, USA). Attenuated total reflection Fourier-transform infrared (ATR-FTIR) spectra were obtained in the range 4000-500 cm$^{-1}$ using a Thermo Nicolet iS50 instrument. Thermogravimetric analyses (TGA) were acquired using a Shimadzu DTG-60/60H instrument. The samples were heated from 30 to 600 °C at a heating rate of 5 °C min$^{-1}$ and a nitrogen flow of 50 cm$^3$ min$^{-1}$. Powder X-ray diffraction (PXRD) analyses were carried out on a Bruker D8 Advance X-ray diffractometer with CuKα (λ = 1.5418 Å) within a 2θ range of 10-100° and indexed with the Joint Committee on Powder Diffraction Data (JCPDS) cards from International Center for Diffraction Data and the crystallite size (D) calculated from Scherrer's equation 1:

$$D = \frac{K\lambda}{\beta \cos\theta} \tag{1}$$

where K is the proportionality constant; λ is the X-ray wavelength; β is the peak width in full width at half maximum (FWHM); and θ is the Bragg's diffraction angle.

Transmission electron microscopy (TEM) was performed on a JEOL JEM-1011 instrument operated at an accelerating voltage of 80 kV. Magnetic properties were measured in a magnetometer Quantum Design MPMS3 using a SQUID (superconducting quantum interference device) sensor. Zeta potential (ζ-potential) and hydrodynamic diameter measurements were carried out with a Zetasizer Nano ZS90 instrument by Malvern Instruments. The ζ-potential of MNP-CP[5]A (0.075 mg mL$^{-1}$) was measured in KNO$_3$ solution (0.01 mol L$^{-1}$) at pH values ranging from 2 to 10. The hydrodynamic diameter was measured in PBS (phosphate buffered saline) buffer at pH = 7.4. Ultraviolet-visible (UV-Vis) absorption spectra were acquired using a Cary 60 UV-Vis spectrophotometer Agilent.

### Synthesis of the ammonium carboxylate-substituted pillar[5] arene salt (CP[5]A)

The synthesis of water-soluble ammonium carboxylate-substituted pillar[5]arene salt (CP[5]A) was carried out in five steps following a procedure described in the literature[51-53] with modifications (Scheme S1, Supplementary Information

(SI) section). Briefly, under stirring in an inert atmosphere, paraformaldehyde (44.9 mmol) and trifluoride diethyl etherate (14.68 mmol) was added to a 1,4-dimethoxybenzene (14.48 mmol) solution in 1,2-dichloroethane (30 mL). Then, the solution was poured in MeOH and the solid formed collected by filtration, yielding 92% of compound **1** as a yellowish solid after purification. A solution of compound **1** (1.83 mmol) and boron tribromide (89.28 mmol) in dry CH$_2$Cl$_2$ was stirred under an inert atmosphere and at room temperature for 4 days, then H$_2$O was poured to the reaction mixture and left under stirring for additional 3 days. The solid formed was collected by filtration, washed with H$_2$O and dried under vacuum to yield compound **2** (90%) as a white solid after purification. To a mixture of compound **2** (1.65 mmol) and K$_2$CO$_3$ (20.97 mmol) in CH$_3$CN, KI (30 mg) and ethyl bromoacetate (17.67 mmol) were added and the reaction mixture was left under reflux for 15 h. The mixture was filtered, concentrated under vacuum, and the residue purified by crystallization, yielding 41% of compound **3**. To a solution of compound **3** (6.93 mmol) in EtOH, an aqueous solution NaOH (40%) was added, and the reaction was stirred under reflux for 10 h. The mixture was concentrated under vacuum and dissolved in H$_2$O. Then HCl was added and the resulting solid collected, washed with H$_2$O, and dried under vacuum to yield compound **4** (P[5]A, 55%). A solution of **4** (0.168 mmol) in H$_2$O was stirred with NH$_4$OH for 5 h. The mixture was concentrated under vacuum and the final product, CP[5]A, obtained in 100% yield as a yellow solid. ATR-FTIR ν / cm$^{-1}$ 1571, 1497, 1429, 1399, 1330, 1198, 1063; $^1$H NMR (500 MHz, D$_2$O) δ 6.73 (s, 10H, Ar-H), 4.28 (s, 20H, CH$_2$), 3.84 (s, 10H, CH$_2$); $^{13}$C NMR (125 MHz, D$_2$O) δ 177.07, 129.45, 128.8, 115.06, 67.81, 29.40.

### Preparation of magnetic nanoparticles (MNP)

Magnetic nanoparticles (MNP) were synthesized by Massart method with minor modifications, followed by a nitric acid treatment to achieve maghemite phase.[14,54] Briefly, under N$_2$ atmosphere an aqueous solution containing both FeCl$_2$.4H$_2$O (50 mL, 0.33 mol L$^{-1}$) and FeCl$_3$ (50 mL, 0.66 mol L$^{-1}$) were added to an aqueous NH$_4$OH solution (450 mL, 30%) under vigorous mechanical stirring. The reaction mixture remained under N$_2$ atmosphere for 1 h at 90 °C. Then, the black solid was separated from the solution using a magnet and washed with distilled water until pH = 7.0. The nanoparticles were oxidized to obtain the maghemite phase by treating the resulting solid with HNO$_3$ (300 mL, 2 mol L$^{-1}$) under mechanical stirring during 15 min. The supernatant was removed and a solution of Fe(NO$_3$)$_3$ (75 mL, 1 mol L$^{-1}$) was added to the nanoparticles.

After 30 min under reflux, the supernatant was removed and another aliquot of HNO₃ (300 mL, 2 mol L⁻¹) was added and the mixture remained under stirring for further 15 min. The nanoparticles were isolated using magnetic decantation, washed with acetone (4×), and dried under vacuum (8 h) to yield a brownish solid (3.67 g) named MNP.

## Preparation of the MNP-CP[5]A

The MNP surface was functionalized with CP[5]A based on a procedure described in the literature with modifications.[14] The magnetic nanoparticles (0.8 g) were dispersed in deionized water (96 mL) using an ultrasound bath for 15 min, then HCl (0.4 mL, 12 mol L⁻¹) was added up to pH = 2.0. The dispersion was mechanically stirred and then ammonium carboxylate-substituted CP[5]A salt (0.48 mmol) dissolved in deionized water was quickly added in one portion to the suspension. After 72 h of stirring at RT, the brownish solid was collected with a magnet, washed with distilled water up to pH = 7.0, and purified using a dialysis bag of cellulose membrane (14 kDa, Sigma-Aldrich). The final product was dried under vacuum for 8 h and named MNP-CP[5]A (1.1 g).

## Magnetic hyperthermia capability of MNP-CP[5]A

The capacity of MNP-CP[5]A to generate heat (magnetic hyperthermia) in an AMF was investigated using a magnetic hyperthermia induction system (Nanoscale Biomagnetics DM2-s53) equipped with vacuum shield as thermal insulation and an optic fiber temperature probe. The nanoparticles were placed in a 2 mL vial sample holder containing PBS buffer (pH = 7.4), and their final concentrations were 1, 5, 10, 15, and 20 mg mL⁻¹. After the introduction of each vial on the middle of the instrument coil, the samples were subjected to AMF at fixed frequency (f) of 307 kHz and field amplitude (H) of 200 Oe during 50 min. The heating temperature was detected and plotted against time.

## Interaction between DOX and CP[5]A

¹H NMR spectrum of an equimolar (2.45 μmol) mixture of CP[5]A and DOX were recorded in D₂O (700 μL) at RT. The stoichiometry of the interaction between CP[5]A and DOX was evaluated by the method of continuous variation (Job plot), through UV-Vis spectroscopy data. The UV-Vis experiments were carried out by mixing different volumes of two aqueous solutions of CP[5]A and DOX in the same concentrations ([CP[5]A] = [DOX] = $3 \times 10^{-5}$ mol L⁻¹). The mixture of both solutions was carried out keeping the

same final volume in the quartz cuvette (3 mL). The molar proportion between the two compounds changed from 0 to 1.

## DOX loading of MNP-CP[5]A

MNP-CP[5]A (0.100 g) dispersed in 80 mL of a DOX water solution (0.0175 mg mL⁻¹) light-protected was gently shaken (100 rpm) for 24 h at RT. After this period, MNP-CP[5]A was collected using a magnet and the excess of DOX was removed from the solid through several washing steps. The solid was dried under vacuum at RT for 8 h, yielding MNP-CP[5]A-DOX. The supernatants were collected to calculate drug-loading efficiency. The amount of DOX loaded into MNP-CP[5]A-DOX was determined using the DOX standard curve from the difference between the initial DOX concentration (0.0175 mg mL⁻¹) in solution and the remaining DOX concentration in the supernatant after a period of 24 h in contact with the MNP-CP[5]A plus washing waters. DOX standard curve was constructed according to the measurement of series of concentrations of DOX solutions in water (1, 10, 20, 30, 40, 50 mg L⁻¹) at λ = 483 nm (Figure S7, SI section). The calculated amount of DOX loaded in the nanocarrier was 9.5 mg g⁻¹. DOX-loading efficiency was calculated using equation 2 where $m_{DOX-Loaded}$ is the mass of DOX in the nanocarrier after loading and $m_{DOX-Initial}$ is the initial mass of DOX used. The DOX-loading efficiency for MNP-CP[5]A-DOX was 68%.

$$\text{DOX-loading efficiency (\%)} = m_{DOX-Loaded} / m_{DOX-Initial} \times 100 \quad (2)$$

## DOX release behavior as function of temperature without AMF application

The experiments were carried out at 37 °C (body temperature) and 45 °C (hyperthermia temperature) at physiological pH (7.4). MNP-CP[5]A (15 mg) was placed in a quartz cuvette containing 1 mL of PBS buffer and the dispersed nanoparticles were decanted using a magnet. Then, the cuvette was introduced into the preheated thermoelectric controlled cuvette holder of the UV-Vis spectrophotometer, at 37 or 45 °C. A spectrum was acquired every 10 min during 50 min.

## DOX release behavior of MNP-CP[5]A-DOX in an AMF

A glass vial containing a dispersion of 15 mg of MNP-CP[5]A-DOX in PBS buffer (1 mL, pH 7.4) was introduced in the magnetic induction heating instrument (Nanoscale Biomagnetics DM2-s53). After stabilization of the internal temperature (23-25 °C), the samples were

submitted to an AMF with frequency (f) of 307 kHz and field amplitude (H) of 200 Oe for 0, 10, 20, 30, 40, and 50 min until reaching the temperature of 45 ± 1 °C (hyperthermia temperature). Then, the temperature remained constant by controlling the field amplitude (H). The nanoparticles were magnetically decanted, and the supernatant was collected and analyzed by UV-Vis spectroscopy.

## Results and Discussion

Synthesis and characterization of MNP-CP[5]A

CP[5]A was synthesized in five steps (Scheme S1, SI section).[51-53] 1,4-Dimethoxybenzene (**1**), a hydroquinone derivative, was cyclized by reacting with paraformaldehyde in the presence of a Lewis acid $BF_3 \cdot OEt_2$, and the solvent 1,2-dichloroethane as template. Then, dimethoxypillar[5]arene (**2**) was O-demethylated with boron tribromide, and the pillar[5]arene (**3**) reacted with ethyl bromoacetate through $S_N2$ reaction to obtain the ester pillar[5]arene (**4**). The carboxylic acid pillar[5]arene (**5**) was obtained after refluxing it with NaOH aqueous solution followed by an acidification reaction. Finally, the reaction of (**5**) with $NH_4OH$ provided the water-soluble ammonium carboxylate-substituted pillar[5]arene salt, CP[5]A (**6**). ^{1}H and ^{13}C NMR spectra of CP[5]A in $D_2O$ confirmed the formation of the macrocycle (Figures S1 and S2, SI section).

Superparamagnetic magnetite nanoparticles were prepared by coprecipitation employing Massart method[54] followed by nitric acid treatment to obtain maghemite phase, which is more stable than magnetite at ambient conditions.[55] In addition, the acid treatment was carried out because the functionalization process with CP[5]A was better succeeded under acid conditions (pH = 2), which certainly would oxidize and change the nanoparticle surface during the functionalization process. Therefore, the nanoparticles were subjected to a previous controlled oxidation.

The ATR-FTIR spectra of MNP, CP[5]A and MNP-CP[5]A are depicted in Figure 1. In the MNP spectrum, the broad band at 3200-3550 cm$^{-1}$ region and the intense band at 1615 cm$^{-1}$ are associated to OH groups and water present on the surface of MNP, whereas the bands in the range of 1300-1255 cm$^{-1}$ are of nitrate anions from the acid treatment. The intense bands at 623 and 529 cm$^{-1}$ are related to the stretching vibrations of Fe–O bonds of maghemite bulk.[14] These bands were also observed in the MNP-CP[5]A spectrum. The grafting of CP[5]A onto MNP was confirmed by the bands at 1715, 1608, and 1400 cm$^{-1}$, which are assigned to $\upsilon(C=OOH)$, $\upsilon(C=OO^-)_{asym}$ and

$\upsilon(C–OO^-)_{sym}$ stretching vibrations, respectively. The bands associated to nitrate anions disappeared in the spectrum of MNP-CP[5]A, indicating these groups were replaced by the carboxylate groups of CP[5]A. The band at 1715 cm$^{-1}$ indicates some CP[5]A remains in the acid form due to acid pH used in the synthesis. However, a displacement ($\Delta\upsilon_{C=OOH} = 5$ cm$^{-1}$) of this band in comparison to carbonyl band at 1720 cm$^{-1}$ of acid pillar[5]arene (P[5]A, Figure S3, SI section) indicates the acid groups of P[5]A might be coordinated to Fe$^{III}$ ion.[56]
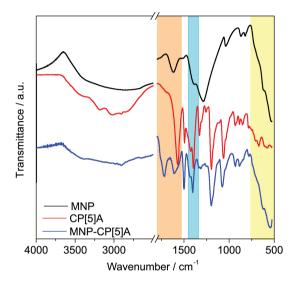


**Figure 1.** ATR-FTIR spectra of MNP-CP[5]A and its precursors.

Thermogravimetric analyses (TGA) exhibit two main decomposition steps for MNP-CP[5]A and its precursors (Figure S4, SI section). The initial weight loss at approximately 100 °C may be related to elimination of adsorbed solvent molecules on the surface of all materials. The second weight loss for MNP, CP[5]A and MNP-CP[5]A was 7.3, 34.2, and 67.6% at temperatures ranging from 100 to 600 °C. This second weight loss for MNP-CP[5]A starts at approximately 150 °C due to decomposition of CP[5]A molecules. From TGA results, the calculated amount of CP[5]A anchored onto the surface of MNP was 0.27 mg of CP[5]A *per* mg of MNP-CP[5]A. Therefore, CP[5]A was successfully grafted onto MNP surface.

Powder X-ray diffraction (PXRD) patterns of MNP and MNP-CP[5]A are shown in Figure 2. We would expect the formation of maghemite phase due to the oxidation process of the MNP with nitric acid. However, because PXRD patterns of maghemite ($\gamma$-Fe$_2$O$_3$, JCPDS 39-1346) and magnetite (Fe$_3$O$_4$, JCPDS 19-629) phases are very similar we cannot discharge the formation of both phases in the materials. PXRD also shows the MNP does not undergo relevant changes in its crystallinity after CP[5]A coating. Using Scherrer's equation 1, the calculated crystallite

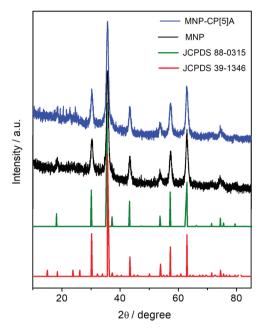sizes of the nanoparticles were 11 nm for both MNP and MNP-CP[5]A.



**Figure 2.** PXRD of MNP-CP[5]A and MNP.

TEM images (Figures 3 and S5, SI section) show a spherical shape and uniform size distribution of MNP and MNP-CP[5]A. The particle size distribution (PSD) is centered at 12 and 13 nm for MNP and MNP-CP[5]A, respectively, therefore, no significant size distribution changes were detected after coating MNP with CP[5]A molecules.

Figure 4 shows the magnetic characterization for MNP and MNP-CP[5]A performed at RT. The inset in Figure 4 shows the magnetization at zero magnetic field is lower than the instrument accuracy at zero magnetic field accuracy. Therefore, the absence of hysteresis, coercivity and remnant magnetization indicate the superparamagnetic nature of the materials at T = 300 K. The saturation value of the magnetization at this temperature corresponds to approximately 42.4 and 25.8 emu g$^{-1}$ for MNP and MNP-CP[5]A, respectively, confirming both materials are mostly composed by maghemite.[57] The lower saturation value of the magnetization for MNP-CP[5]A compared to MNP is due to the presence of CP[5]A as an organic diamagnetic matter.

ζ-Potential of MNP-CP[5]A and MNP was measured to evaluate the surface modification of the magnetic nanoparticles after coating with CP[5]A as well the colloidal stability of the materials as function of pH (2-10). The experiments were carried out using the same concentration of both materials (0.075 mg mL$^{-1}$). From Figure 5, the values of ζ-potentials for both materials decrease
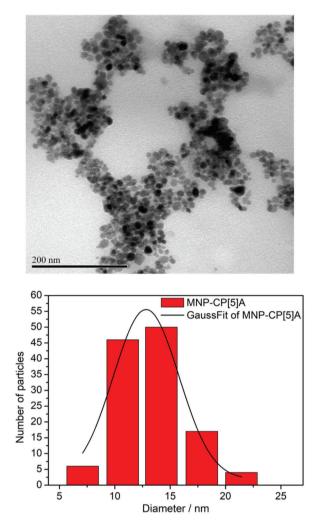




**Figure 3.** TEM image and particle size distribution of MNP-CP[5]A.

with increasing pH (> 8) due to the deprotonation of hydroxyl and carboxyl groups of MNP and MNP-CP[5]A, respectively. In contrast, upon acidification of MNP dispersion (black curve) (pH < 7), ζ-potential increased and reached positive values (+30 mV at pH = 2), most likely because of protonation of the hydroxyl groups present on MNP surface. The same tendency is observed for MNP-CP[5]A (blue curve) at pH < 7, in which ζ-potential values increased with decreasing pH values due to protonation of the carboxyl groups of CP[5]A. However, for MNP-CP[5]A, ζ-potential is negative in all acid pH range measured (−15 mV at pH = 2.4). The negative nature of MNP-CP[5]A in acid medium can be attributed to the high amount of carboxylate groups of CP[5]A grafted on MNP surface, decreasing the pH of the isoelectric point of MNPs.[56,58,59] ζ-potential values at pH = 7.4 for MNP and MNP-CP[5]A are +0.46, and −44.48 mV, respectively. The isoelectric point (IEP) for the bare MNP is 7.5, therefore, very close to 7.4, which means this material is an unstable colloid at
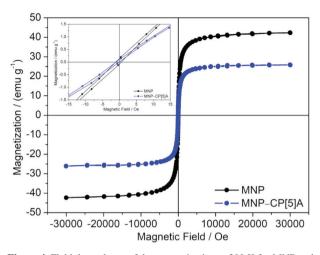
**Figure 4.** Field dependence of the magnetization at 300 K for MNP and MNP-CP[5]A. The inset figure shows a magnification around zero field at the same temperature.

physiological conditions. MNP-CP[5]A, however, shows highly negative value of ζ-potential at pH = 7.4, which is desirable for biomedical applications because there is no nanoparticle aggregation at physiological conditions. The average hydrodynamic diameter obtained from dynamic light scattering (DLS) measurements at pH = 7.4 decreases from 898 nm for the bare MNP to 248 nm for MNP-CP[5]A (Figure S6, SI section) confirming, therefore, coating the SPIONs with CP[5]A decreases particle aggregation, corroborating the results obtained by ζ-potential measurements.
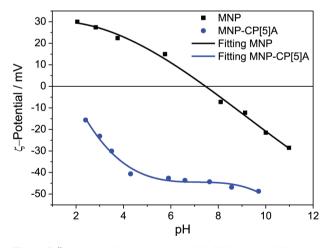


**Figure 5.** ζ-Potential of the nanocarrier MNP-CP[5]A and MNP.

## Concentration-dependent heating of MNP-CP[5]A in an AMF

To verify the potential use of MNP-CP[5]A as a magnetic hyperthermia induced agent, we investigated the magnetic heating capacity as function of the MNP-CP[5]A concentration in PBS buffer. Figure 6 shows the results

of heating capacity for several concentrations under the same conditions of magnetic field, i.e., 200 Oe of amplitude and with a frequency of 307 kHz. It is worth to note that field strength and frequency product was $4.9 \times 10^9$ A m$^{-1}$ s$^{-1}$, which is considered safe to be used in physiological applications.[60] For concentrations of 10, 15, and 20 mg mL$^{-1}$ of MNP-CP[5]A, it takes 25, 12, and 8 min to reach the hyperthermia temperature of 45 °C, respectively (Figure 6). For the concentrations of 1 and 5 mg mL$^{-1}$ of MNP-CP[5]A, the dispersions did not reach the temperature of 45 °C, even for the longest acquisition time (50 min).
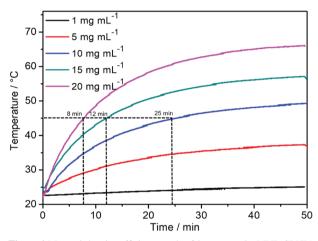


**Figure 6.** Magnetic heating efficiency study of the nanocarrier MNP-CP[5]A (PBS buffer, pH = 7.4) in different concentrations.

From the magnetic heating efficiency results shown in Figure 6 it is possible to calculate the specific absorption rate (SAR) of the MNP-CP[5]A agent. The SAR is the magnetic energy converted into heat, normalized by both, the time and the mass of the magnetic nanoparticles, during the hyperthermia essays.[61] The SAR depends on the size, shape, saturation of magnetization, concentration, and interparticle magnetic interaction in the dispersion.[62] To calculate the SAR of the samples it was considered the initial slope method:

$$SAR = (m_{MNP} C_{MNP} + m_L C_L / m_{MNP}) \times (dT/dt) \quad (3)$$

where $m_{MNP}$ and $m_L$ are the mass (kg) of the nanoparticles and of the liquid, respectively; $C_{MNP}$ and $C_L$ are the specific heat (J kg$^{-1}$ K$^{-1}$) of the nanoparticles and the liquid; and dT/dt is the initial slope of the temperature *versus* time curve (Figure 6), which is the temperature increase *per* time (K s$^{-1}$).[63] The dT/dt values (Figure 6) used for SAR calculation were: 0.020 K s$^{-1}$ (5 mg mL$^{-1}$), 0.043 K s$^{-1}$ (10 mg mL$^{-1}$), 0.048 K s$^{-1}$ (15 mg mL$^{-1}$), and 0.075 K s$^{-1}$ (20 mg mL$^{-1}$).

The SAR is linearly dependent on the frequency (f) and quadratically dependent on the field amplitude (H) of the AMF applied. To compare heating efficiency at different experimental conditions of amplitude and frequency of the magnetic field, intrinsic loss power (ILP) quantities were also calculated. ILP parameter allows a more suitable comparison than SAR of the results obtained in this work to the ones reported in the literature,[64] because ILP is an intrinsic quantity. ILP (in nH $m^2$ $kg^{-1}$) values were calculated using equation 4:[10]

$$ILP = SAR/fH^2 \qquad (4)$$

The calculated SAR and ILP values are displayed in Figure 7. SAR values decrease with increasing concentration of MNP-CP[5]A. According to Deatsch and Evans,[63] the concentrations of MNP in the dispersions can drastically affect the two main microscopy heating process, namely Brown and Néel relaxations times. The authors argue that in high concentration range of MNP, due to the decrease in the mean interparticle distances, some collective effects take place. One of them is the increase of dipolar interparticle interaction, as the interparticles mean distance decreases, which affects the magnetic anisotropy of the system, therefore, changing the Néel relaxation time.[65,66] In addition, as the nanoparticles get closer to each other agglomeration can occur, increasing Brown relaxation process substantially. Therefore, because SAR decreases with increasing concentration of MNP-CP[5]A, we suggest that most likely the total relaxation time is increasing.[65,66]
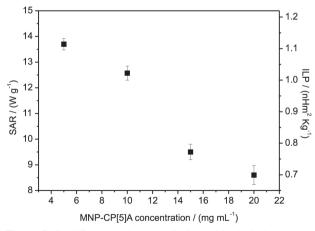


**Figure 7.** Specific absorption rate (SAR) and intrinsic loss power (ILP) values for MNP-CP[5]A dispersed in PBS buffer in different concentrations (5, 10, 15, 20 mg mL$^{-1}$).

The calculated ILP values for MNP-CP[5]A ranged from 0.8 to 1.2 nH $m^2$ $kg^{-1}$ depending on the concentration of the nanoparticles (Figure 7). The ILP values reported in the literature[67] for commercial colloids of iron nanoparticles

(ferrofluid) are in the range of 0.2 to 3.1 nH $m^2$ $kg^{-1}$. Therefore, the obtained values for MNP-CP[5]A synthesized in this work are very suitable for a possible application of this nanoplatform as a hyperthermia agent.

### Investigation of DOX⊂CP[5]A interaction

$^1$H NMR spectroscopy experiments were carried out to investigate the interaction between CP[5]A and DOX (DOX⊂CP[5]A), Figure 8. The spectra of pure DOX[68,69] and CP[5]A were also included in Figure 8. On addition of equimolar amount of DOX (2.45 µmol) to a solution of CP[5]A (2.45 µmol) in $D_2O$, broadening of the signals occurred indicating the presence of more than one species undergoing slow exchange on the $^1$H NMR time scale (Figure 8b). The resonances for the hydrogens $H_c$, $H_b$, $H_d$, and $H_j$ in DOX were shifted downfield from 7.71, 7.52, 7.44, and 5.50 ppm to 7.95, 7.66, and 5.73 ppm, respectively, indicating interaction with CP[5]A. The chemical shifts of all the other hydrogen atoms in both the DOX and CP[5]A in the DOX⊂CP[5]A changed dramatically as well.

To investigate the stoichiometry of this interaction, a Job plot, a method of continuous variation, was employed using UV-Vis spectroscopy (Figure 9) by monitoring the intensity of the electronic absorption band of DOX at $\lambda = 483$ nm at different molar fractions of the components (Figure 9b). Figure 9 shows two isosbestic points, in which the absorption intensity at 228 and 277 nm is constant throughout the experiment. The presence of isosbestic points is good evidence for the conversion of free components (DOX and CP[5]A) into complex DOX⊂CP[5]A. The maximum point in Job plot curve at 0.5 indicates a 1:1 binding stoichiometry between CP[5]A and DOX. Furthermore, the parabolic shape of the plot indicates an evenly distributed equilibrium.[70]

### DOX release from MNP-CP[5]A

DOX loading efficiency in the nanocarrier MNP-CP[5]A-DOX was 68% with a loading capacity of 9.5 mg g$^{-1}$ of MNP-CP[5]A nanoparticles, which is ten times higher than the one obtained by our group in a previous work[24] using magnetic nanoparticles functionalized with β-cyclodextrin (MNP-βCD) loaded with DOX, e.g. 0.81 mg g$^{-1}$ of MNP-βCD nanoparticles. DOX release studies in PBS buffer (pH = 7.4) were conducted in different temperatures to evaluate the efficiency of AMF stimulus (Figure 10). The experiments were carried out at 37 °C (body temperature) and 45 °C (hyperthermia temperature) without AMF application using a thermostatic cuvette to control the temperature of the dispersions. Also, DOX
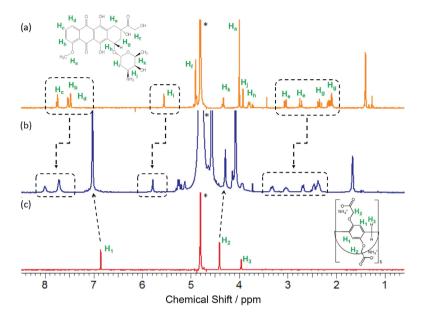
**Figure 8.** $^1$H NMR spectra (25 °C, 500 MHz, $D_2O$) of (a) pure DOX (3.5 mmol $L^{-1}$); (b) DOX⊂CP[5]A (1:1) (3.5 mmol $L^{-1}$); and (c) pure CP[5]A (3.5 mmol $L^{-1}$).
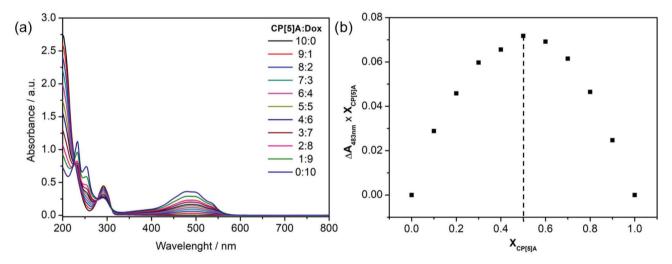


**Figure 9.** (a) UV-Vis spectra of mixtures of two different volumes of CP[5]A and DOX water solutions ([CP[5]A]=[DOX] = $3 \times 10^{-5}$ mol $L^{-1}$) at RT; (b) Job plot of DOX⊂CP[5]A complex obtained from the UV-Vis data of Figure 9a.

release studies were carried out in an AMF at 45 °C in PBS buffer (pH = 7.4).

In the absence of AMF, DOX release is low (Figure 10), reaching an amount of 1.8 µg mL$^{-1}$ (1.9%) and 3.3 µg mL$^{-1}$ (2.3%) at 37 and 45 °C within 50 min, respectively. However, DOX release increased to 8.2 µg mL$^{-1}$ (5.7%) within 50 min in an AMF.

In an AMF the temperature increase of MNP-CP[5]A-DOX dispersion is due to Néel and Brown relaxation processes, in which the interaction of the magnetic moments of the nanoparticles with the alternating magnetic field generates thermal energy.[24,63] Because DOX is interacting through supramolecular interactions with CP[5]A, DOX release may be related to Brown relaxation process,[24] in which the heating is generated by the friction
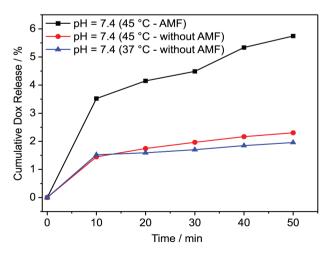


**Figure 10.** DOX release profile for MNP-CP[5]A-DOX in PBS buffer (pH = 7.4) in the presence and absence of an AMF as a function of time.

between the MNP surface and the medium. This ultimately will decrease DOX interaction with CP[5]A and DOX is released.

Although the percentage of DOX released in the AMF is low (5.7%) relative to the total percentage of DOX loaded in MNP-CP[5]A-DOX, in terms of concentration, however, it corresponds to 0.0141 mmol L$^{-1}$. This concentration is compatible to the IC$_{50}$ (drug concentration required to inhibit cell growth by 50%) of various types of cancer cell lines in which DOX is used (Table 1). Therefore, the result of DOX release in an AMF from the nanocarrier MNP-CP[5]A-DOX indicates this material can be applied as a potential candidate for chemo-hyperthermia therapy.

**Table 1.** IC$_{50}$ for different doxorubicin responsive cell lines

| Cell line | Tissue sub-type | IC$_{50}$[a] / (mmol L$^{-1}$) |
|---|---|---|
| KGN | ovary | 0.00616 |
| SUP-B15 | lymphoblastic, leukemia | 0.00745 |
| MCF7 | breast | 0.00984 |
| DU-4475 | breast | 0.00966 |
| ESS-1 | endometrium | 0.011 |
| 786-0 | kidney | 0.0112 |
| PA-1 | ovary | 0.0117 |
| MV-4-11 | leukemia | 0.0117 |

[a]The conditions employed to determine IC$_{50}$ (drug concentration required to inhibit cell growth by 50%) values were obtained from reference 71.

## Conclusions

In summary, the design, synthesis, characterization, and operation of a nanodevice based on magnetic nanoparticles coated with carboxylate-substituted pillar[5]arene (CP[5]A) aiming target chemo-hyperthermia therapy were investigated. Superparamagnetic nanoparticles of 12 nm (TEM) were successfully obtained by the coprecipitation method. The surface modification of MNPs with CP[5]A improved the colloidal stability of the MNPs. Moreover, from Job plot, CP[5]A can interact with DOX in water forming a complex DOX⊂CP[5]A in 1:1 binding stoichiometry. MNP-CP[5]A showed high DOX loading and magnetic heating capacities.

The temperature increase by using different heating sources, e.g. thermoelectric or alternating magnetic field stimuli, can trigger DOX release from the nanocarrier. However, the amount of DOX release at 45 °C using AMF stimulus is two and a half times higher than in the absence of AMF in the same temperature. Improvement of DOX release in AMF occurs mainly due to the friction between the surface of the loaded nanocarrier and the solution (Brown relaxation process), which will increase the temperature of the solution (magnetic hyperthermia process) weakening the binding between the pillar[5]arene and the drug. In addition, MNP-CP[5]A-DOX displayed an amount of DOX release compatible with IC$_{50}$ of many kinds of cancer cells. Therefore, MNP-CP[5]A-DOX can be considered a potential drug delivery system.

## Supplementary Information

Supplementary information (CP[5]A synthesis scheme, $^1$H and $^{13}$C NMR CP[5]A data, ATR-FTIR spectra of P[5]A and MNP-CP[5]A, thermogravimetric analysis MNP-CP[5]A, TEM and PSD of MNP, DLS measurements of MNP and MNP-CP[5]A, and calibration curves of DOX in water and PBS buffer) is available free of charge at http://jbcs.sbq.org.br as PDF file.

## Acknowledgments

## References

1. Beik, J.; Abed, Z.; Ghoreishi, F. S.; Hosseini-Nami, S.; Mehrzadi, S.; Shakeri-Zadeh, A.; Kamrava, S. K.; *J. Controlled Release* **2016**, *235*, 205.

2. DeNardo, G. L.; DeNardo, S. J.; *Cancer Biother. Radiopharm.* **2008**, *23*, 671.

3. Périgo, E. A.; Hemery, G.; Sandre, O.; Ortega, D.; Garaio, E.; Plazaola, F.; Teran, F. J.; *Appl. Phys. Rev.* **2015**, *2*, 41302.

4. Behrouzkia, Z.; Joveini, Z.; Keshavarzi, B.; Eyvazzadeh, N.; Aghdam, R. Z.; *Oman Med. J.* **2016**, *31*, 89.

5. van der Zee, J.; *Ann. Onc.* **2002**, *13*, 1173.

6. Silva, J. S. F.; Silva, J. Y. R.; De Sá, G. F.; Araújo, S. S.; Filho, M. A. G.; Ronconi, C. M.; Santos, T. C.; Júnior, S. A.; *ACS Omega* **2018**, *3*, 12147.

7. Kumar, C. S. S. R.; Mohammad, F.; *Adv. Drug Delivery Rev.* **2011**, *63*, 789.

8. Das, P.; Colombo, M.; Prosperi, D.; *Colloids Surf., B* **2019**, *174*, 42.

9. Moros, M.; Idiago-López, J.; Asín, L.; Moreno-Antolín, E.; Beola, L.; Grazú, V.; Fratila, R. M.; Gutiérrez, L.; de la Fuente, J. M.; *Adv. Drug Delivery Rev.* **2019**, *138*, 326.

10. Wildeboer, R. R.; Southern, P.; Pankhurst, Q. A.; *J. Phys. D: Appl. Phys.* **2014**, *47*, 495003.

11. Hauser, A. K.; Wydra, R. J.; Stocke, N. A.; Anderson, K. W.; Hilt, J. Z.; *J. Controlled Release* **2015**, *219*, 76.

12. Kuo, C.; Liu, T.; Chan, T.; Tsai, S.; Hardiansyah, A.; Huang, L.; Yang, M.; Lu, R.; Jiang, J.; Yang, C.; Lin, C.-H.; Chiu, W.-Y.; *Colloids Surf., B* **2016**, *140*, 567.

13. Santos, E. C. S.; dos Santos, T. C.; Guimarães, R. B.; Ishida, L.; Freitas, R. S.; Ronconi, C. M.; *RSC Adv.* **2015**, *5*, 48031.

14. da Silva, G. B.; Marciello, M.; Morales, M. D. P.; Serna, C. J.; Vargas, M. D.; Ronconi, C. M.; Costo, R.; *J. Braz. Chem. Soc.* **2017**, *28*, 731.

15. Mohammed, L.; Gomaa, H. G.; Ragab, D.; Zhu, J.; *Particuology* **2017**, *30*, 1.

16. Ventola, C. L.; *P&T®* **2017**, *42*, 742.

17. Caster, J. M.; Patel, A. N.; Zhang, T.; Wang, A.; *WIREs Nanomed. Nanobiotechnol.* **2017**, *9*, 1.

18. Laurent, S.; Forge, D.; Port, M.; Roch, A.; Robic, C.; Vander Elst, L.; Muller, R. N.; *Chem. Rev.* **2008**, *108*, 2064.

19. Fan, H.; Li, B.; Shi, Z.; Zhao, L.; Wang, K.; Qiu, D.; *Ceram. Int.* **2018**, *44*, 2345.

20. Kostiv, U.; Patsula, V.; Šlouf, M.; Pongra, I. M.; Škokić, S.; Radmilović, M. D.; Pavičić, I.; Vrček, I. V.; And, S. G.; Horák, D.; *RSC Adv.* **2017**, *7*, 8786.

21. Silveira, G. Q.; Ronconi, C. M.; Vargas, M. D.; San Gil, R. A. S.; Magalhães, A.; *J. Braz. Chem. Soc.* **2011**, *22*, 961.

22. Gutiérrez, L.; Romero, S.; da Silva, G. B.; Costo, R.; Vargas, M. D.; Ronconi, C. M.; Serna, C. J.; Veintemillas-Verdaguer, S.; Del Puerto Morales, M.; *Biomed. Tech.* **2015**, *60*, 417.

23. Rojas, J. M.; Gavilán, H.; del Dedo, V.; Lorente-Sorolla, E.; Sanz-Ortega, L.; da Silva, G. B.; Costo, R.; Perez-Yagüe, S.; Talelli, M.; Marciello, M.; Morales, M. P.; Barber, D. F.; Gutiérrez, L.; *Acta Biomater.* **2017**, *58*, 181.

24. Santos, E. C. S.; Watanabe, A.; Vargas, M. D.; Tanaka, M. N.; Garcia, F.; Ronconi, C. M.; *New J. Chem.* **2018**, *42*, 671.

25. Silveira, G. Q.; Vargas, M. D.; Ronconi, C. M.; *J. Mater. Chem.* **2011**, *21*, 6034.

26. Silveira, G. Q.; da Silva, R. S.; Franco, L. P.; Vargas, M. D.; Ronconi, C. M.; *Microporous Mesoporous Mater.* **2015**, *206*, 226.

27. Benyettou, F.; Fahs, H.; Elkharrag, R.; Bilbeisi, R. A.; Asma, B.; Rezgui, R.; Motte, L.; Magzoub, M.; Brandel, J.; Olsen, J.; Piano, F.; Gunsalus, K. C.; Platas-Iglesias, C.; Trabolsi, A.; *RSC Adv.* **2017**, *7*, 23827.

28. Benyettou, F.; Alhashimi, M.; Connor, M. O.; Pasricha, R.; Brandel, J.; Traboulsi, H.; Mazher, J.; Olsen, J.; Trabolsi, A.; *ACS Appl. Mater. Interfaces* **2017**, *9*, 40006.

29. Chin, S. F.; Makha, M.; Raston, L.; Saunders, M.; *Chem. Commun.* **2007**, 1948.

30. Sathiyajith, C. W.; Shaikh, R. R.; Han, Q.; Zhang, Y.; Meguellati, K.; Yang, Y. W.; *Chem. Commun.* **2017**, *53*, 677.

31. Cragg, P. J.; *Isr. J. Chem.* **2018**, *58*, 1194.

32. Song, N.; Kakuta, T.; Yamagishi, T.; Yang, Y.; Ogoshi, T.; *Chem* **2018**, *4*, 2029.

33. Li, Q. L.; Sun, Y.; Ren, L.; Wang, X.; Wang, C.; Li, L.; Yang, Y. W.; Yu, X.; Yu, J.; *ACS Appl. Mater. Interfaces* **2018**, *10*, 29314.

34. Li, H.; Wei, R.; Yan, G. H.; Sun, J.; Li, C.; Wang, H.; Shi, L.; Capobianco, J. A.; Sun, L.; *ACS Appl. Mater. Interfaces* **2018**, *10*, 4910.

35. Yu, G.; Zhou, J.; Shen, J.; Tang, G.; Huang, F.; *Chem. Sci.* **2016**, *7*, 4073.

36. Hu, X.; Liu, X.; Zhang, W.; Qin, S.; Yao, C.; Li, Y.; Cao, D.; Peng, L.; Wang, L.; *Chem. Mater.* **2016**, *28*, 3778.

37. Chang, Y.; Yang, K.; Wei, P.; Huang, S.; Pei, Y.; Zhao, W.; Pei, Z.; *Angew. Chem., Int. Ed.* **2014**, *53*, 13126.

38. Jiang, L.; Huang, X.; Chen, D.; Yan, H.; Li, X.; Du, X.; *Angew. Chem., Int. Ed.* **2017**, *56*, 2655.

39. Xiao, T.; Zhong, W.; Xu, L.; Sun, X.; Hu, X.; Wang, L.; *Org. Biomol. Chem.* **2019**, *17*, 1336.

40. Yao, Y.; Xue, M.; Chen, J.; Zhang, M.; Huang, F.; *J. Am. Chem. Soc.* **2012**, *134*, 15712.

41. Zhou, J.; Chen, M.; Diao, G.; *ACS Appl. Mater. Interfaces* **2014**, *6*, 18538.

42. Tan, L.; Li, H.; Zhou, Y.; Zhang, Y.; Feng, X.; Wang, B.; Yang, Y.-W.; *Small* **2015**, *11*, 3807.

43. Huang, X.; Du, X.; *ACS Appl. Mater. Interfaces* **2014**, *6*, 20430.

44. Tan, L.-L.; Li, H.; Qiu, Y.-C.; Chen, D.-X.; Wang, X.; Pan, R.-Y.; Wang, Y.; Zhang, S. X.-A.; Wang, B.; Yang, Y.-W.; *Chem. Sci.* **2015**, *6*, 1640.

45. Sun, Y. L.; Yang, Y. W.; Chen, D. X.; Wang, G.; Zhou, Y.; Wang, C. Y.; Stoddart, J. F.; *Small* **2013**, *9*, 3224.

46. Wu, M.; Yan, H.; Gao, J.; Cheng, Y.; Yang, J.; Wu, J.; Gong, B.; Zhang, H.; Yang, Y.; *ACS Appl. Mater. Interfaces* **2018**, *10*, 34655.

47. Li, X.; Han, J.; Wang, X.; Zhang, Y.; Jia, C.; Qin, J.; Wang, C.; Wu, J.-R.; Fang, W.; Yang, Y.-W.; *Mater. Chem. Front.* **2019**, *3*, 103.

48. Zhang, H.; Wu, J. R.; Wang, X.; Li, X.-S.; Wu, M.-X.; Liang, F.; Yang, Y.-W.; *Dyes Pigm.* **2019**, *162*, 512.

49. Tian, M. M.; Chen, D. X.; Sun, Y. L.; Yang, Y. W.; Jia, Q.; *RSC Adv.* **2013**, *3*, 22111.

50. Wu, M.-X.; Gao, J.; Wang, F.; Yang, J.; Song, N.; Jin, X.; Mi, P.; Tian, J.; Luo, J.; Liang, F.; Yang, Y.-W.; *Small* **2018**, *14*, 1704440.

51. Ogoshi, T.; Aoki, T.; Kitajima, K.; Fujinami, S.; Yamagishi, T.; Nakamoto, Y.; *J. Org. Chem.* **2011**, *76*, 328.

52. Li, H.; Chen, D.-X.; Sun, Y.-L.; Zheng, Y. B.; Tan, L.-L.; Weiss, P. S.; Yang, Y.-W.; *J. Am. Chem. Soc.* **2013**, *135*, 1570.

53. Li, C.; Shu, X.; Li, J.; Chen, S.; Han, K.; Xu, M.; Hu, B.; Yu, Y.; Jia, X.; *J. Org. Chem.* **2011**, *76*, 8458.

54. Massart, R.; *IEEE Trans. Magn.* **1981**, *17*, 1247.

55. Costo, R.; Bello, V.; Robic, C.; Port, M.; Marco, J. F.; Puerto Morales, M.; Veintemillas-Verdaguer, S.; *Langmuir* **2012**, *28*, 178.

56. Tombácz, E.; Szekeres, M.; Hajdú, A.; Tóth, I. Y.; Bauer, R. A.; Nesztor, D.; Illés, E.; Zupkó, I.; Vékás, L.; *Period. Polytech., Chem. Eng.* **2014**, *58*, 3.

57. Rahman, M.; Usman, M.; Ullah, A.; Zulfiqar, S.; *J. Korean Phys. Soc.* **2014**, *65*, 1925.

58. Szekeres, M.; Tóth, I. Y.; Illés, E.; Hajdú, A.; Zupkó, I.; Farkas, K.; Oszlánczi, G.; Tiszlavicz, L.; Tombácz, E.; *Int. J. Mol. Sci.* **2013**, *14*, 14550.

59. Atacan, K.; Kursunlu, A. N.; Ozmen, M.; *Mater. Sci. Eng., C* **2019**, *94*, 886.

60. Hergt, R.; Dutz, S.; *J. Magn. Magn. Mater.* **2007**, *311*, 187.

61. Nemati, Z.; Alonso, J.; Khurshid, H.; Phan, M. H.; Srikanth, H.; *RSC Adv.* **2016**, *6*, 38697.

62. Shubitidze, F.; Kekalo, K.; Stigliano, R.; Baker, I.; *J. Appl. Phys.* **2015**, *117*, 094302.

63. Deatsch, A. E.; Evans, B. A.; *J. Magn. Magn. Mater.* **2014**, *354*, 163.

64. de Mello, L. B.; Varanda, L. C.; Sigoli, F. A.; Mazali, I. O.; *J. Alloys Compd.* **2019**, *779*, 698.

65. Piñeiro-Redondo, Y.; Bañobre-López, M.; Pardiñas-Blanco, I.; Goya, G.; López-Quintela, M. A.; Rivas, J.; *Nanoscale Res. Lett.* **2011**, *6*, 383.

66. Linh, P. H.; Van Thach, P.; Tuan, N. A.; Thuan, N. C.; Manh, D. H.; Phuc, N. X.; Van Hong, L.; *J. Phys.: Conf. Ser.* **2009**, *187*, 6.

67. Kallumadil, M.; Tada, M.; Nakagawa, T.; Abe, M.; Southern, P.; Pankhurst, Q. A.; *J. Magn. Magn. Mater.* **2009**, *321*, 1509.

68. Wang, Y.; Wang, R.; Lu, X.; Lu, W.; Zhang, C.; Liang, W.; *Pharm. Res.* **2010**, *27*, 361.

69. Lu, J.; Zhao, W.; Huang, Y.; Liu, H.; Marquez, R.; Gibbs, R. B.; Li, J.; Venkataramanan, R.; Xu, L.; Li, S.; Li, S.; *Mol. Pharm.* **2014**, *11*, 4164.

70. Corda, E.; Hernandez, M.; Sanchez-Cortes, S.; Sevilla, P.; *Colloids Surf., A* **2018**, *557*, 66.

71. https://www.cancerrxgene.org/translation/Drug/133, accessed on February 15, 2019.